https://doi.org/10.5194/egusphere-2026-4142
Preprint. Discussion started: 30 July 2026

A physics-based morphometric model to explain the emergence of landslide rupture geometry and to identify hillslope transience

Philippe Steer[1,2], Lucas Pelascini[1], Laurent Longuevergne[1]

[1]Univ. Rennes, CNRS, Géosciences Rennes - UMR 6118, 35000 Rennes, France
[2]Institut universitaire de France (IUF)

Correspondence to: Philippe Steer (philippe.steer@univ-rennes.fr)

Abstract. Like earthquakes or other rupture processes, landslide tends to universally follow some specific geometrical scaling laws and size distributions. Numerical models have attempted to explain the emergence of these universal laws, putting forward mainly the role of hillslope strength and shape. The main difficulty that models are facing is that the geometry of the surface rupture of a landslide, or of large population of landslides, is not a priori known and must often be guessed using assumptions about the rupture shape, depth, and angle. Here, we develop an analytical solution that defines an optimal rupture depth, below each point of a topography, associated with an optimal rupture angle. This defines a rupture surface that daylights downslope the rupture point. Landslides are then defined as clusters of unstable neighbours sharing the same daylight point. The geometry of the surface rupture of the landslide is then simply defined by the optimal rupture depth at each point belonging to the landslide. Applying this model, coined scaLr (slope curvature analysis for Landslide rupture) to the Central Range of Taiwan, we show it can produce landslide area-volume and area-depth relationships with power-law exponents roughly consistent with observed ones. The distribution of landslide length-to-width ratio is also consistent with the range of observed values and exhibit a distribution similar to an Inverse-Gamma. The distribution of landslide area exhibits a power-law decay for large landslides and no clear rollover is obtained despite a break in slope below a cutoff area. However, the power-law decay tends to be in the lower part of the range of observed values. Amalgamating modelled landslides does however produce more acceptable exponents, which suggests that the difference between modelled and observed landslides might partly results from inherent amalgamation in landslide catalogues. Last, we show that the optimal rupture depth also represents a morphometric index to assess landscape transience along hillslopes. In Taiwan, we tend to observe deeper expected ruptures along streams locally characterized by high river steepness as well on the aggressive side of migrating divides, as identified by the χ index. The optimal rupture depth therefore offers complementary information to fluvial metrics, such as river steepness or the χ index, and to hillslope metrics such as Gilbert's metrics.

1 Introduction

Landslides represent a major natural hazard and contribute significantly to surface erosion and to fluxes of organic carbon in areas characterized by steep slopes and high relief (Keefer, 1994; Malamud et al., 2004; Hilton et al., 2008; Croissant et al.,

https://doi.org/10.5194/egusphere-2026-4142
Preprint. Discussion started: 30 July 2026

2019, 2021; Marc et al., 2019; Lavé et al., 2023). Despite a large diversity of failure mechanisms, rupture surface geometries, hillslope materials, or triggering factors, landslides tend to follow some universal size distributions and geometrical scaling laws (Hovius et al., 1997; Malamud & Turcotte, 1999; Stark & Hovius, 2001; Malamud et al., 2004; Guzzetti et al., 2005; Van Den Eeckhaut et al., 2007; Stark & Guzzetti, 2009; Larsen et al., 2010; Tanyas et al., 2017; Jeandet et al., 2019; Tebbens, 2020). Landslide surface area distributions follow a negative power-law scaling for larger landslides, while smaller landslides are potentially underrepresented compared to this power-law scaling, even if this latter is actively debated (e.g., Stark & Hovius, 2001; Tanyas et al., 2019; Bernard et al., 2021). It is also observed that landslide depth and landslide volume increase as a power-law of landslide area (e.g., Hovius et al., 1997; Guzzetti et al., 2009; Larsen et al., 2010; Jaboyedoff et al., 2020). Understanding the processes and factors controlling the geometrical scaling and size-distribution of landslides remain a scientific but also a societal challenge, as it could provide relevant information on the frequency and size of future landslides and therefore on the associated hazards and risks. If the physical processes and parameters controlling the geometry of one or few landslides can be determined (e.g., Samyn et al., 2012; Kuo et al., 2009; Lucas et al., 2011; Argentin et al., 2022), this offers limited insights for the understanding of the scaling of large populations of landslides, as triggered during large earthquakes or rainfall events.

Several studies have developed non-case specific models to explain the emergence of these size distributions and scaling laws for large populations of landslides, such as sandpile models (e.g., Bak, 1996; Hergarten et al., 2002), cellular automata models (e.g., Pelletier et al., 1997), mechanical models (e.g., Klar et al., 2011; Lehmann & Or, 2012; Alvioli et al., 2014; Milledge et al., 2014; Bellugi et al., 2015) or probabilistic-mechanistic models (e.g., Densmore et al., 1998; Stark & Guzzetti, 2009; Frattini & Crosta, 2013; Gallen et al., 2015; Jeandet et al., 2019; Campforts et al., 2020; Medwedeff et al., 2020). It is suggested that the following topographical and mechanical factors strongly influence the size-distribution of landslides: 1) material cohesion leads to the emergence of a rollover position for small landslides; 2) the resistance to rupture initiation and propagation (and its potential depth-variability) control the power-law exponent for intermediate to large landslides; 3) the finite-size of hillslopes bounds the maximum size of landslides and 4) the length, width and height distributions of hillslopes lead to a progressive underrepresentation of the largest landslides compared to the power-law scaling. Moreover, secondary factors, such as the depth of open fractures favored by topographic stresses (Li & Moon, 2021), weathering (Alberti et al., 2022) or the strength and depth of vegetation roots (e.g., Casadei & Dietrich, 2003; Dietrich et al., 2007; Phillips et al., 2021) also impact the occurrence and size distributions of bedrock and regolith landslides. On top of these inferences, the spatial extent, and the clustering of low-strength patches along hillslopes probably limit the effective maximum size of landslides (Pelletier et al., 1997; Frattini & Crosta, 2013; Alvioli et al., 2014; Bellugi et al., 2021). Moreover, hillslopes are affected by transient dynamics related to river-hillslope coupling and potentially induced by local baselevel variations and divide migration, leading to heterogeneous slope and concavity distribution from the hillslope toe to the crest (Hurst et al., 2019; Soen et al., 2026). The impact of such slope heterogeneities, on the susceptibility, geometry and size-distributions of landslides, remains an open question.

https://doi.org/10.5194/egusphere-2026-4142
Preprint. Discussion started: 30 July 2026

However, many of these inferences are based on probabilistic-mechanistic models which include assumptions about the expected geometry of landslides and their rupture geometry. For instance, Jeandet et al. (2019) or Medwedeff et al. (2020) compute the distribution of unstable landslide depth or length, respectively, but not directly of landslide area or volume (distribution of landslide area is obtained in Jeandet et al. (2019) by applying a depth-to-area scaling law). On the contrary, case-specific models are generally applied to a priori known or inferred geometry of the landslide surface rupture (e.g., Kuo et al., 2009; Moretti et al., 2015; Argentin et al., 2022; Gong et al., 2023; Medwedeff et al., 2025). This type of approach is, however, generally intractable when considering large populations of landslides. Except for landslide catalogs obtained from high-resolution topographic differencing (Bernard et al., 2021; Ju et al., 2023; Clark et al., 2024; Jones et al., 2025), most catalogs of co-seismic or rainfall-triggered landslides do not provide direct information on the depth of the surface rupture as they are generally derived from 2D optical images. In this case, landslide depth is often inferred based on the area-to-depth scaling law (e.g., Larsen et al., 2010)

In this study, we explore the ability of a new simple morphometric model to simulate the geometry of landslide surface rupture as an emergent property, not prescribed by modelling assumptions. This new model extends the approach of Jeandet et al. (2019) by explicitly simulating the lateral extent of landslides, made of clusters of neighborhood unstable pixels. We coined this model morphometric as it is mostly based on topographic analysis. In the following, we first describe the new model in the methods section. In the results, we show that landslides, with geometrical properties generally respecting the established scaling laws observed in nature, self-emerge from the model when applied to a natural topography. We then discuss the main benefits and limits of this new model, compared to previous approaches. Once this new model established, we then showthe ability of this model to provide, as a byproduct, a new geomorphological metrics to assess the expected rupture depth of unstable slopes. This expected rupture depth proves to be informative to identify potential divide migration or transience in landscape dynamics, complementary to other fluvial- or hillslope-based metrics (e.g., Kirby & Whipple, 2012; Perron & Royden, 2013; Willett et al., 2014; Soen et al., 2026).

2 Methods and study area

Three physical-based strategies for slope stability modelling applied to digital elevation models (DEM) are generally considered. The first strategy relies on a limit equilibrium analysis applied to a whole landslide surface rupture, assuming that a landslide behaves as one or a series of rigid bodies (e.g., Lehmann & Or, 2012; Milledge et al., 2014). The second strategy rather considers a reduced-complexity approach: it identifies an initial failure point (i.e., an unstable or the most unstable point), from which a landslide is generated assuming the geometrical shape (e.g., plane, cone, concave surface) of the rupture surface and a direction of rupture propagation, either uphill or downhill (e.g., Densmore et al., 1998; Gallen et al., 2014; Jeandet et al., 2019; Campforts et al., 2020). The first strategy is more robust and physically consistent, but it is also more computationally expensive and requires knowledge of the geometry of the rupture surface. A third, intermediate, strategy consists in determining all the unstable points and clustering them in continuous patches of unstable areas to identify the

https://doi.org/10.5194/egusphere-2026-4142
Preprint. Discussion started: 30 July 2026

geometry and size of individual landslides (e.g., Alvioli et al., 2014). The model we develop here belongs to this third type of modelling strategy and we coin it scaLr for slope curvature analysis for Landslide rupture. It extends previous modelling approaches by 1) automatically determining the most unstable depth (i.e., the optimal depth) for each point of a DEM, 2) by associating this optimal rupture depth to a planar rupture surface that must daylight downhill, and 3) by imposing that a landslide consists in a neighborhood of unstable points which must daylight at the same location along the hillslope. We below describe these different steps of this new landslide model,

2.1 A simple mechanical model for hillslope stability

The model developed here is based on an 1D infinite slope form of the Mohr-Coulomb failure, neglecting the role of pore pressure or seismic wave acceleration. Under this assumption, a classical expression for the safety factor is:

$$F = \frac{c + \mu\sigma_n}{\tau} \tag{1}$$

Where σ_n and τ are the normal and tangential stresses to the rupture plane, c the cohesion and $\mu = \tan\varphi$ the coefficient of friction and φ the internal friction angle. The safety factor represents the ratio between resisting and driving stresses, and $F > 1$ indicates a stable slope, while $F = 1$ or $F < 1$ respectively indicates a critical or unstable state that should lead to slope failure. Due to the simplicity of our modelling strategy, there is no destabilization term in the expression of the safety factor (Eq. 1), whether due to pore pressure change or seismic wave acceleration. Therefore, as we aim to simulate large populations of co-seismic or rainfall-triggered landslides, we rely on an equivalent or apparent approach. In our model, slope destabilization during these events is obtained by considering a reduced value of cohesion compared to its pristine value. In a reduced complexity approach, this allows us to account for a lowering of F (here induced by an apparent decrease in mechanical strength rather than by introducing additional forces reducing F), which is expected during earthquakes or rainfall events. We refer the readers to Appendix A for model derivation accounting for pore pressure.

Under a uniaxial stress (without considering lateral stresses and resistance), due to the gravitational body force, the normal and tangential stresses are $\sigma_n = \rho g h \cos\theta \cos\theta$ and $\tau = \rho g h \cos\theta \sin\theta$, with h the depth (positive), θ the rupture angle, g the gravitational acceleration and ρ the rock density. Developing equation (1) leads to:

$$F = \frac{c}{\rho g h \cos\theta \sin\theta} + \frac{\mu}{\tan\theta} \tag{2}$$

This classical expression of the safety factor illustrates the competition between cohesion and column weight and between the friction angle and the local angle of the rupture surface. We define z as the topographic elevation and x the horizontal coordinate along the hillslope of the considered point, hereinafter referred to as point R (for rupture). In the following, we assume that the local rupture surface is planar and that it daylights at point D (for daylight), located at a relative horizontal distance Δx from - and a relative elevation Δz below – point R. In turn, the tangent of the rupture angle $\tan\theta$ can also be expressed as the ratio between $\Delta z - h$, the difference of elevation between the tip and the top of the rupture plane, and Δx, the horizontal distance, leading to:

https://doi.org/10.5194/egusphere-2026-4142
Preprint. Discussion started: 30 July 2026

$$F = \frac{c}{\rho g h}\frac{\Delta x^2 + (\Delta z - h)^2}{\Delta x(\Delta z - h)} + \mu\frac{\Delta x}{\Delta z - h} \tag{3}$$

It is important to note that even if the model defines a finite rupture plane, between points R&D, slope stability is yet only assessed at point R using an infinite slope formalism. This represents a physical approximation, which yet holds as in the following the rupture surface geometry of landslides will only be defined on a series of unstable points R, irrespectively of the planes linking each couple of points R&D.

2.2 Determining the most unstable or optimal rupture depth

We now wish to find the optimal depth that leads to the most unstable rupture plane. Indeed, determining clusters of unstable points and their depths will enable us to define the horizontal extent and surface geometry of the landslides, respectively. Assuming a uniform value of cohesion and friction angle and known values of Δx and Δz, equation (3) is only dependent on the depth h. The derivative of F relative to h can be readily obtained,

$$\frac{dF}{dh} = \frac{c}{\rho g h}\left(\frac{\Delta x^2 + (\Delta z - h)^2}{\Delta x(\Delta z - h)^2} - \frac{2(\Delta z - h)}{\Delta x(\Delta z - h)} - \frac{\Delta x^2 + (\Delta z - h)^2}{\Delta x(\Delta z - h)h}\right) + \mu\frac{\Delta x}{(\Delta z - h)^2}, \tag{4}$$

and in turn solving for the roots of $\frac{dF}{dh}$ provides with analytical expressions of this optimal rupture depth. Equation (4) admits two roots, which are the depths h_{min} leading to the minimum value of the safety factor F_{min}:

$$h_{min} = -\frac{c(\Delta x^2 + \Delta z^2) + \Delta x\sqrt{c(c + \mu\rho g\Delta z)(\Delta x^2 + \Delta z^2)}}{\mu\rho g\Delta x^2 - c\Delta z}, \tag{5}$$

and,

$$h_{min} = -\frac{c(\Delta x^2 + \Delta z^2) - \Delta x\sqrt{c(c + \mu\rho g\Delta z)(\Delta x^2 + \Delta z^2)}}{\mu\rho g\Delta x^2 - c\Delta z} \tag{6}$$

Only one of these two roots is positive and corresponds to the optimal rupture depth below the considered point. Except for very high values of cohesion ($c > \mu\rho g\Delta x^2/\Delta z$), this is likely the second root (Eq. 6) that is positive. This can be tested numerically in a model.

https://doi.org/10.5194/egusphere-2026-4142
Preprint. Discussion started: 30 July 2026

2.3 Determining where the rupture plane daylights

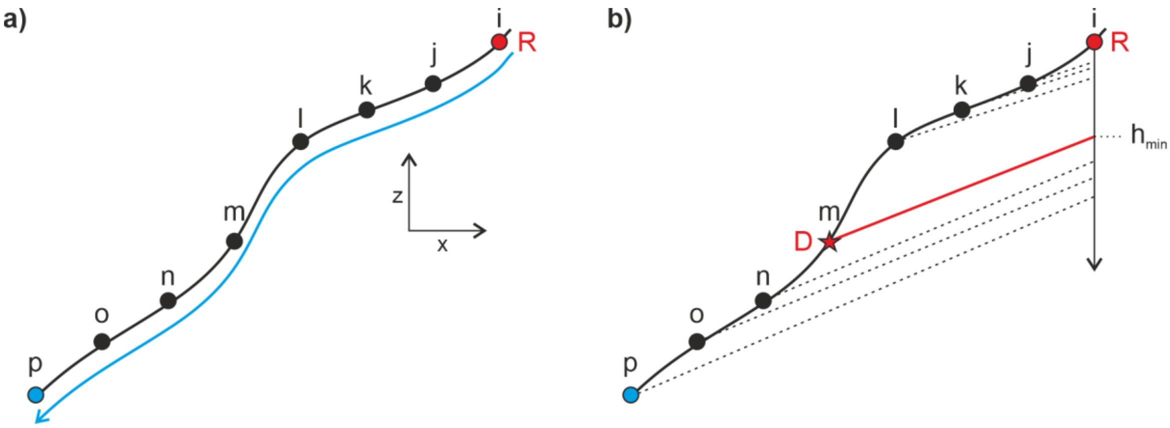

Figure 1: Schematic scheme, showing a cross-section through a hillslope, and illustrating how the optimal rupture line and depth are defined for a potential rupture point. We here briefly describe the different steps. a) First, a potential rupture point R (label i) is selected and the hydrological path to the river as well as a list of downhill points are computed using a single flow algorithm. b) Each downhill point (j to p) is considered as a potential daylight point D and is linked to point R by a potential rupture plane starting at an optimal depth $h_{min}(i, j \text{ to } p)$ below point R. The associated safety factors $F_{min}(i, j \text{ to } p)$ are computed, and the most unstable rupture plane (i.e., lowest safety factor) associated with the potential point D (ranging from j to p) is selected, leading to the final couple R&D and to the optimal value of h_{min} and F_{min}. In this case point m if the daylight point D.

For a rupture point R, the optimal rupture depth h_{min} still depends on Δx and Δz (i.e., on the rupture angle), and therefore on the location of point D, where the surface rupture daylights. This also means that changing the location of point D will lead to a different value of h_{min}. Practically every couple of points R&D of a DEM could be tested and lead to a value of h_{min} and F. However, this solution is computationally expensive and could lead to couples of points which do not belong to the same hillslope. For each point R, we therefore restrict the search for the most unstable point D only to locations downstream of point R (i.e., along the same hillslope). The list of downhill points is obtained by hydrological ordering, using the single flow algorithm based on the steepest slope criterion (O'Callaghan and Mark, 1984). The obtained hydrological path can be described by a direct acyclic graph, allowing to efficiently perform downstream operations along 1D paths (e.g., Schwanghart & Scherler, 2014, Steer et al., 2021). Points belonging to fluvial or colluvial channels are excluded from the list of downhill points. This is achieved by removing point with a drainage area greater than a threshold A_c that is approximatively taken between 10^4 and 10^6 m^2 for colluvial channels and between 10^5 and 10^7 m^2 for fluvial channels (e.g., Montgomery & Foufoula-Georgiou, 1993; Lague & Davy, 2003; Medwedeff et al. 2020).

Practically, for a rupture point R, values of h_{min} and F_{min} are computed for each potential point D chosen along the downhill list of points. The final point D is chosen as the one leading to the minimum value of F_{min}, and the associated optimal depth h_{min} is then readily obtained (by imposing the values of Δx and Δz in equations (5,6)). This algorithm is performed for every point of the DEM, therefore leading to a final set of couples of R&D points and their associated optimal rupture depth h_{min} and rupture surface geometry.

https://doi.org/10.5194/egusphere-2026-4142
Preprint. Discussion started: 30 July 2026

2.4 Determining landslide geometry by clustering unstable points

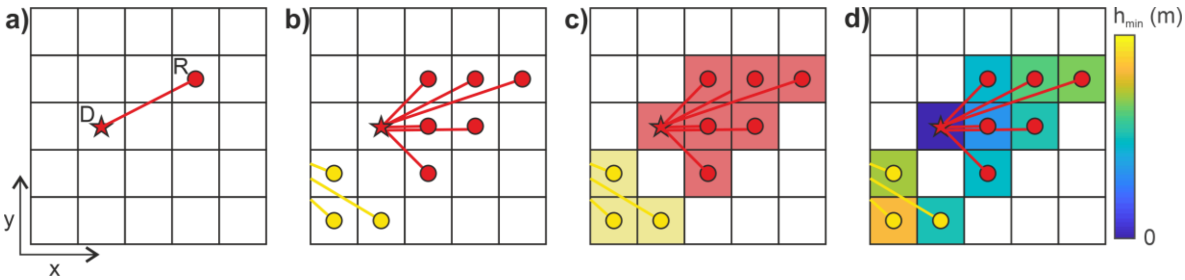

Figure 2: Schematic sketch, in map view, illustrating the emergence of landslide in our model, as a clustering process identifying each rupture point R associated with the same daylight D as a unique landslide. a) Identification of a first unstable rupture point R (red cercle) and its daylight point D (red star). b) identification of all the unstable points R and their point D. c) labelling of unstable points R sharing the same point D as a unique landslide. Here, two landslides are identified, in red and yellow. d) computation of the optimal rupture depth h_{min} (given by the color scale) for all the points R, defining in turn the geometry of the landslide surface rupture.

As reflected by equation (2), inferring the value of the safety factor requires determining values for both the rupture depth and angle. By enforcing that the most unstable rupture plane (i.e., rupture plane angle) and rupture depth are chosen, the developed algorithm implicitly proposes an efficient solution to this classical conundrum of slope stability assessments. However, determining unstable points and their associated rupture depth and surface geometry does not provide with an identification of potential landslides. This can be achieved by the clustering of spatially continuous patches of unstable neighborhood points (e.g., Alvioli et al., 2014). In the following, we therefore assume that a landslide is defined as a continuous patch of unstable points, but we also add the condition that all these unstable points must share the same daylight point D to be identified as a landslide. This last condition imposes a strong constraint on the final geometry of the rupture surface. However, as already mentioned in section (2.1), the final landslide rupture surface geometry is defined by the optimal rupture depth h_{min} below each unstable point. The resulting landslide surface rupture is therefore unlikely to be planar. As a side note, the final safety factor F_L of the landslide could be assessed as:

$$F_L = \frac{\sum_i \text{resisting stresses}}{\sum_i \text{driving stresses}} = \frac{\sum_i c + \mu {\sigma_n}^i}{\sum_i \tau^i} = \frac{\sum_i \frac{c}{\rho g} + \mu {h_{min}}^i \cos\theta^i \cos\theta^i}{\sum_i {h_{min}}^i \cos\theta^i \sin\theta^i}, \tag{7}$$

where i is the index of the unstable points of the considered landslide.

https://doi.org/10.5194/egusphere-2026-4142
Preprint. Discussion started: 30 July 2026

2.5 Study area: Central Range of Taiwan

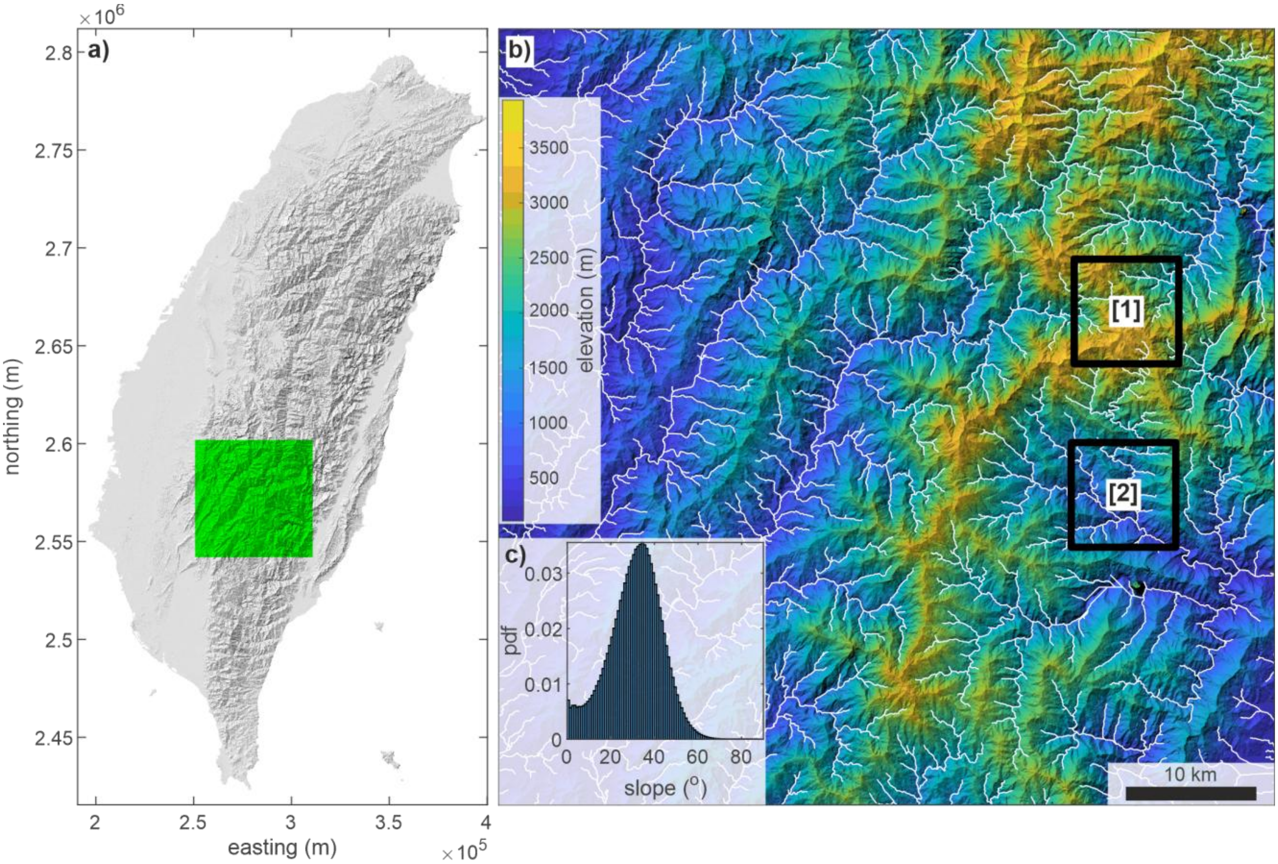

Figure 3: Localisation of the study area in Taiwan. a) Shaded map of relief in Taiwan showing with the green box the localisation of the study area. Coordinates are given in the UTM zone 51Q. b) Map of elevation in the study area, and delineation of the fluvial network (white lines), arbitrarily defined as parts of the landscape with a drainage area above 10^6 m^2. Black squares numbered 1 to 2 are subsets of the DEM which are shown on Fig. 5. c) Probability density function of local slope in the study area, showing a modal slope around 35°. Topography was retrieved from the ALOS Global Digital Surface Model at 30 m of resolution.

To test the model abilities, we apply it in the following to a DEM of the southern part of Taiwan (Fig. 3). The DEM has a resolution of 30 m and was retrieved from the ALOS Global Digital Surface Model. The studied area exhibits steep relief, with a modal slope around 35°. The highest elevation, 3952 m, is reached at Yushan, the highest summit in Taiwan. It is a landslide prone area, as testified by the high spatial density of landslides triggered during typhoon Morakot in 2009 (Marc et al., 2018; Steer et al., 2021). The studied area is mainly located in the Central Range of Taiwan, which is characterized by diverse geological units and lithologies, dominated by slates, shale slates and sandstones. Most maps and topographic analysis performed in this manuscript were obtained using Topotoolbox (Schwanghart & Scherler, 2014; Kearney et al., 2026).

https://doi.org/10.5194/egusphere-2026-4142
Preprint. Discussion started: 30 July 2026

3 Results

3.1 Model sensitivity to mechanical parameters

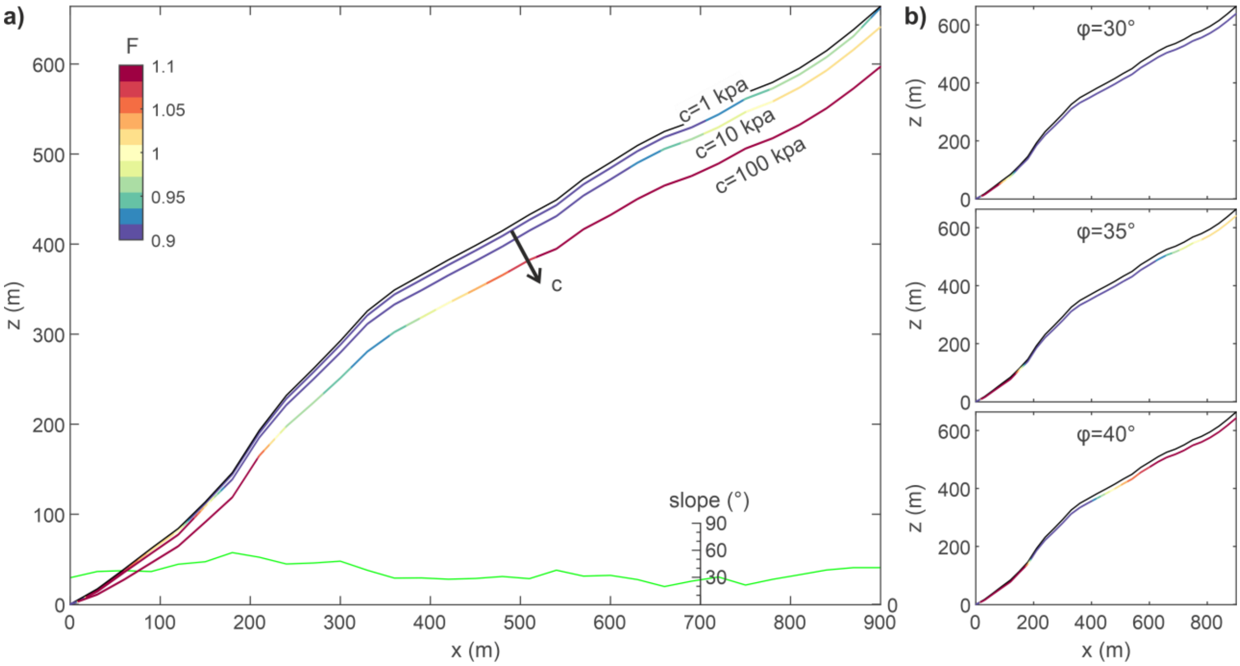

Figure 4: Sensitivity of the modelled hillslope stability to cohesion and friction angle. a) Effect of varying cohesion c, from 1 to 10 and 100 kPa, on the optimal rupture depth. The friction coefficient φ is equal to 35°. The hillslope 1D profile is shown by a black solid line, while the coloured lines show the optimal rupture depth below the topography, with the colour code indicating the value of the associated safety factor F. The local slope is shown by a green line at the bottom of the panel. b) Effect of varying the friction angle φ between 30 (upper panel), 35 (middle panel) and 40° (lower panel). The cohesion c is equal to 10 kPa.

Before applying the model to a 2D topography, we test its sensitivity to the mechanical parameters of the model, the friction angle and cohesion, along a 1D synthetic hillslope profile (Fig. 4). The hillslope profile is obtained by considering a 40° slope perturbed by a correlated noise. At this stage, we simply focus on the optimal rupture depth h_{min} and on the extent of the unstable zones with $F_{min} \leq 1$, without considering the horizontal extent of the resulting landslides. We vary the cohesion c between 1 and 100 kPa, and the friction angle φ between 30 and 40°, which can be considered as reasonable ranges (e.g., Gallen et al., 2015; Jeandet et al., 2019). We first focus on the effect of varying cohesion (Fig. 4a), imposing φ = 35°. As expected from Eq. (4), increasing cohesion increases h_{min}, from about ~5 m for $c = 1$ kPa to ~50 m for $c = 100$ kPa. Increasing cohesion also results in less extended unstable zones, with less optimal rupture depths associated with $F_{min} \leq 1$. This behavior is consistent with previous modelling results showing that cohesion strongly controls hillslope stability at shallow depths. We then focus on the effect of varying the friction angle (Fig. 4b), imposing $c = 10$ kPa. Changing the friction angle has limited impact on h_{min}. However, increasing the friction angle limits the extents of unstable zones, only to location where the local slope is significantly above the friction angle, and where a local rupture plane can be both unstable and daylight

https://doi.org/10.5194/egusphere-2026-4142
Preprint. Discussion started: 30 July 2026

before the hillslope toe. Overall, increasing the friction angle or increasing cohesion leads to a similar localization of unstable zones, by limiting where rupture can occur, while cohesion also strongly impact the depth of the optimal rupture depth.

3.2 Reference model

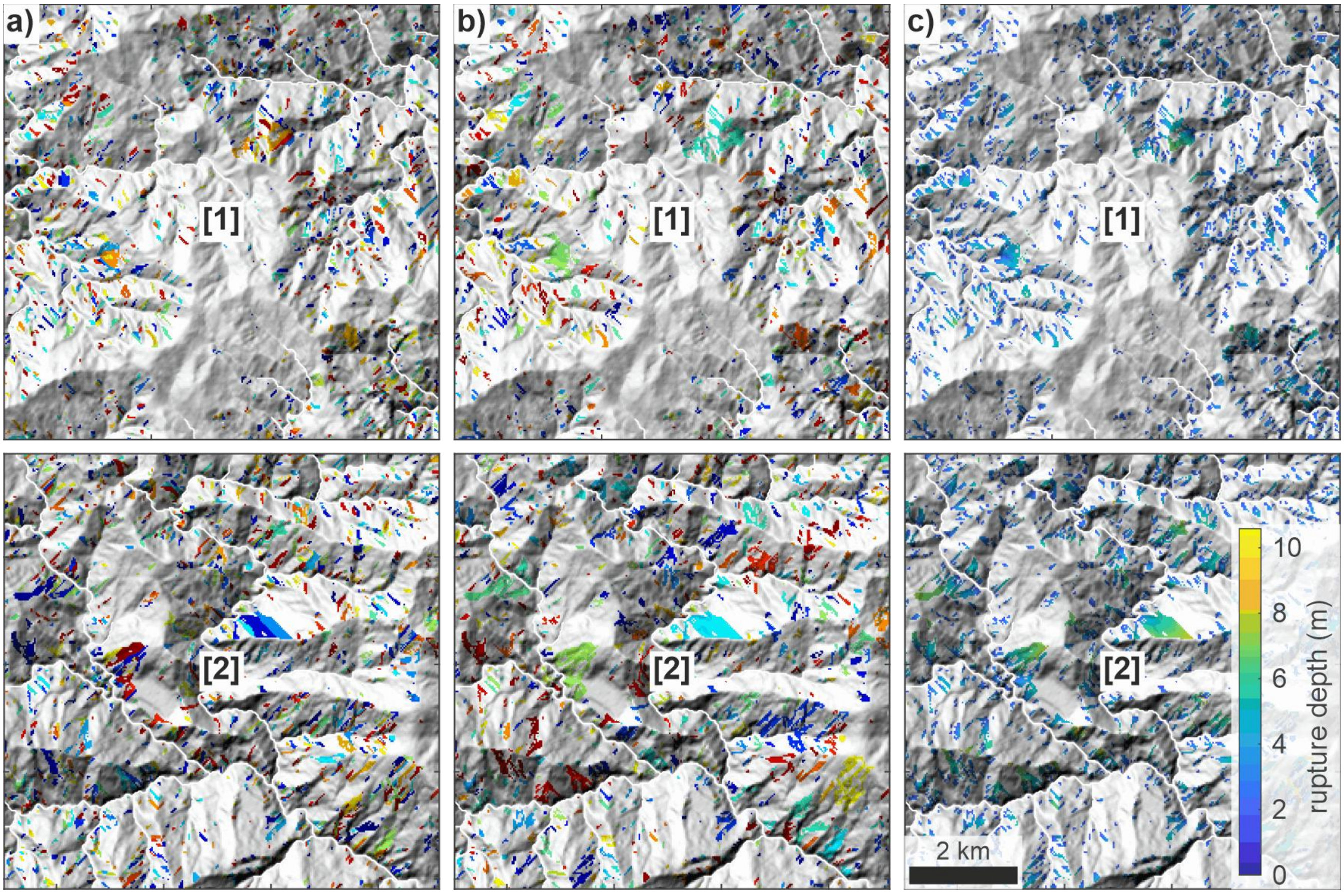

Figure 5: Results of the landslide model shown over the 2 subsets of the studied area. a) Map of the landslide labels given as unique colors for the 3 subsets. b) Same as a, but some landslides have been amalgamated using a 2D connected component algorithm. c) Map of the simulated optimal rupture depths of the landslides.

The reference model is obtained by imposing the values of the two mechanical parameters, with the cohesion $c = 1$ kPa and the friction angle $\varphi = 35^{\circ}$, corresponding to the modal slope of the landscape. Because we are interested in simulating landslides occurring during a triggering event, we choose on purpose to use a low value of cohesion to reflect the lower apparent strength of the hillslopes. Under these conditions, the model automatically identifies a large number of landslides, about ~56,000 landslides, over a total surface area of ~3,600 km^2, with landslides covering about 9 % of the total surface (Fig. 5a). The resulting landslides do consist in continuous patches of unstable points taking a shape qualitatively alike many landslides found in natural systems. Modelled landslides have an area ranging between 900 and 247,500 m^2. Interestingly, a large proportion of modelled landslides have one or several other landslides as direct neighbors. If mapped by an independent

https://doi.org/10.5194/egusphere-2026-4142
Preprint. Discussion started: 30 July 2026

agent (either by hand mapping or by automatic detection), these landslides would have likely been identified as larger landslides, due to amalgamation, and not as several smaller and distinct landslides. We evaluate the potential for amalgamation by using a 2D connected component labeling algorithm, following Bernard et al. (2021), applied to the initial map of landslide labels. This algorithm merges the labels of landslides that are neighbors to each other's, with a 8-connected rule. This offers a second map of "amalgamated" landslide labels (Fig. 5b), with only ~41,000 labeled landslides remaining.

3.3 Landslide volume to area and depth to area relationships

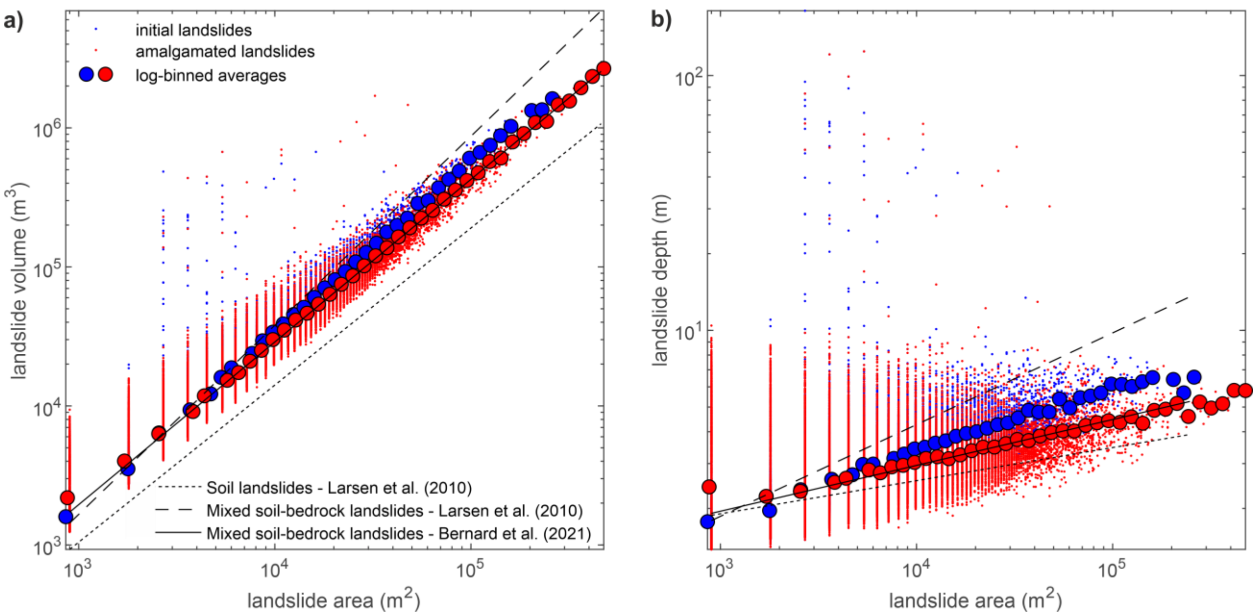

Figure 6: Modelled relationships between landslide area and a) landslide volume and b) depth. Small blue and red dots show the values for all the initial or amalgamated landslides, respectively. Large blue or red circles show the log-binned averages. Previous scaling relationships between landslide area and volume or depth are shown with black lines: continuous lines for the scaling relationships of Bernard et al., 2021, considering mixed soil and bedrock landslides, and dashed or dotted lines for the scaling relationships of Larsen et al., 2010, considering respectively mixed soil and bedrock landslides or soil landslides.

We now focus on the geometrical properties of the modelled landslides. In particular, we investigate the obtained scaling laws between landslide area and volume or depth (Fig. 6). We observe that the amalgamated landslides exhibit a larger range of landslide area, compared to the initial landslides, with the maximum area equal to 460,800 m^2 instead of 247,500 m^2. Due to the amalgamation of landslides, we also observe in proportion less small area landslides associated with large volumes or more large area landslides associated with low volumes.

The modelled relationship between landslide volume V and area A (Fig. 6a) shows a classical power-law behavior $V = \alpha A^{\gamma}$, with α the prefactor and γ the power-law exponent (e.g., Larsen et al., 2010). We find the parameters of this power-law model by performing a classical linear regression in a log-log space applied to the log-binned averages of V. When considering the initial non-amalgamated landslides, we find $\gamma = 1.23$ and $\log \alpha = -0.39$ (with a coefficient of determination $R^2 = 0.99$). When considering the amalgamated landslides, we find a decrease of γ to 1.15 and an increase of $\log \alpha$ to -0.12 ($R^2 = 0.99$).

https://doi.org/10.5194/egusphere-2026-4142
Preprint. Discussion started: 30 July 2026

Performing the regression on the V and A and directly, instead of using the log-binned averages, leads to similar scaling with $\gamma = 1.28$ and $\log\alpha = -0.60$ ($R^2 = 0.92$) or $\gamma = 1.15$ and $\log\alpha = -0.14$ ($R^2 = 0.92$) for the initial or amalgamated landslides, respectively. The power-law scaling relationships obtained with the amalgamated landslides is consistent with $\gamma = 1.17$ and $\log\alpha = -0.22$ the exponent obtained by Bernard et al. (2021) for mixed soil and bedrock landslides, using a LiDAR-derived landslide inventory. The power-law scaling relationships obtained with the initial landslides, with $\gamma = 1.23$ or 1.28 exhibits a higher γ exponent, which is encompassed between 1.17 and 1.36, the exponents reported for mixed soil and bedrock landslides reported by Bernard et al. (2021) and Larsen et al. (2010), respectively. Our results are also consistent with a regional scaling relationship for southern Taiwan obtained on landslides caused by typhoon Morakot with $\log\alpha = -0.69$ and $\gamma = 1.27$ (Chen et al., 2013).

The modelled relationships between A and landslide depth D also show a power-law behavior, despite a greater spread (Fig. 6b). The scaling exponents are 0.23-0.28 or 0.15-0.16 for the initial or amalgamated landslides, respectively, when considering a regression on all the landslides or on the log-binned averages. The exponent obtained for the amalgamated landslides is consistent with 0.16-0.18 obtained by Bernard et al. (2021), while the exponent for the initial landslides is encompassed between 0.16-0.18 (Bernard et al., 2021) and 0.36 by Larsen et al. (2010), for mixed soil and bedrock landslides.

3.4 Landslide length-to-width ratio

We also investigate the length-to-width ratio of the modelled landslides (Fig. 7). Following Taylor et al. (2018), landslide length L and width W are obtained by fitting a 2D ellipsoidal model to the landslide horizontal shape and measuring the length of its major and minor axis, respectively. The ellipse is determined as the one having the same second moment as the region identified by the landslide points. Unsurprisingly, the amalgamated landslides are characterized by a lower ratio L/W than the initial landslides, with mean L/W values of 2.0 and 2.4, respectively. These values are in range with the review of literature performed by Taylor et al. (2018), in their table 1. We also compute the probability density function of the length-to-width ratio $pdf(L/W)$ (Fig. 7b). The $pdf(L/W)$ show a power-law decay for $L/W > 2$ and a potential rollover or plateau-like behavior when $L/W \leq 2$. The power-law decay is stronger for the amalgamated landslides, with an exponent of -5.8, than for the initial landslide, -4.2. We did not test other types of distributions, even if we note that the obtained distributions are also compatible with an Inverse-Gamma distribution, as determined by Taylor et al. (2018).

https://doi.org/10.5194/egusphere-2026-4142
Preprint. Discussion started: 30 July 2026

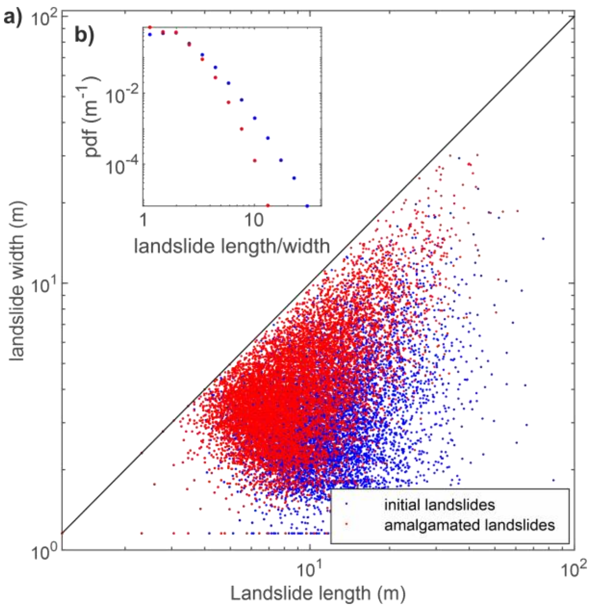

Figure 7: Landslide length to width ratio. a) Modelled relationship between landslide length and landslide width. Small blue and red dots show the values for all the initial or amalgamated landslides, respectively. b) Log-log plot of the probability density function (pdf) or the landslide length-to-width ratio.

3.5 Landslide size distribution

We now focus on the area and volume distributions of the modelled landslides (Fig. 8). We also compare the modelled landslide area distribution with the one obtained by Steer et al. (2020) based on landslides triggered by typhoon Morakot. The modelled landslide area distributions show a power-law decay for large landslides, with a break-off in the scaling for landslides with an area lower than a cutoff around 2.10^4 m^2 (Fig. 8a). We do not observe a clear rollover below this cutoff area, despite an underrepresentation of small landslides compared to the power-law scaling. However, the minimum modelled landslide area is bounded by the DEM cell area of 900 m^2, which is close to classical values of rollover (e.g., Van Den Eeckhaut et al., 2007; Tanyas et al., 2019). For large landslides, the power-law exponents are η=-3.6 and -3.1, for the initial and amalgamated landslides, respectively. These two exponents differ significantly from η =-2.5, the exponent obtained on the landslides observed after typhoon Morakot (Steer et al., 2020). These two exponents are also in the lower range of the spectrum of values of η compiled from various landslide catalogs, between -1.4 to -3.5 with a mean of -2.3 for Van Den Eeckhaut et al. (2007) and between -1.8 to -3.3 with a mean of -2.5 for Tanyas et al. (2019). Yet, we note that, once again, the amalgamated landslides provide a more realistic statistical description for the distribution of landslide area than the initial landslides. The distributions of landslide volume follow similar characteristics than the distribution of landslide area (Fig. 8b). The exponents of the power-law scaling relationships are -2.9 and -2.5 for the initial and amalgamated landslides, respectively. The main difference is that the modelled volume distribution shows a rollover at ~5000 m^3. This is a feature that was also observed by Bernard et al. (2021), though at a much lower volume (i.e., a few tens of m^3).

https://doi.org/10.5194/egusphere-2026-4142
Preprint. Discussion started: 30 July 2026

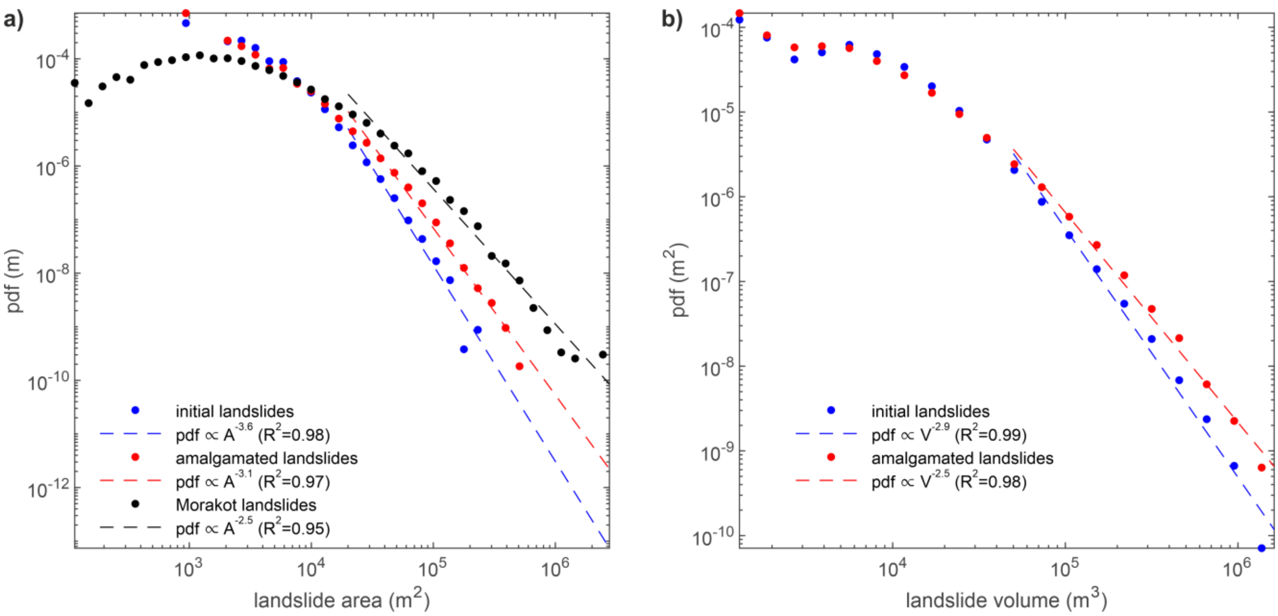

Figure 8: Probability density function (pdf) of a) landslide area and b) landslide volume. Blue and red dots represent the initial and amalgamated landslides, respectively, while the black dots on panel a) represent landslides triggered by typhoon Morakot (Steer et al., 2020). Dashed lines represent the obtained power-law scaling relationships for landslide area or volume greater than 2.10^4 m^2 and 5.10^4 m^3, respectively.

4 Discussion

4.1 Model limitations

The model developed in this study relies on several hypotheses, approximations, and simplifications. First, computation of the safety factor does not integrate any destabilizing term, such as pore pressure change or seismic wave acceleration. If seismic acceleration has not been investigated in this study, we show in Appendix A, that hydrostatic pore pressure can be accounted for in the computation of the optimal rupture depth. In the modelling framework developed here, we rely on the notion of apparent mechanical parameters to account for the reduced hillslope strength during earthquakes or rainfall events. In turn, the resulting low values of cohesion (or friction) used in this study must not be considered as equivalent to pristine values. We also do not consider potential lithological or structural heterogeneities (e.g., cataclinal vs anaclinal slopes), while they exert a strong control on resulting landslide mechanisms and spatial distribution (e.g., Gallen et al., 2015; Huber et al., 2024). However, the developed model is fully compatible with heterogeneous cohesion or friction values, and this could be accounted for in future studies. A second limitation is that we consider an expression for the safety factor based on an infinite slope formalism, while modelling finite-size landslides. Even if this is not the first study to do so (e.g., Jeandet et al., 2019), this represents an approximation. Yet, in our approach, all the points belonging to a landslide must be unstable. This in turn means that each identified landslide, if evaluated with an integration of forces along the rupture surface using the same physical ingredients, is necessarily unstable in a finite slope formalism. We still neglect the potential contributions of lateral forces on

https://doi.org/10.5194/egusphere-2026-4142
Preprint. Discussion started: 30 July 2026

landslide stability, which are essential factors controlling the occurrence and shape of landslides (e.g., Milledge et al., 2014). A third limitation is that the clustering approach used in this study, which consists in clustering all the unstable points R with a rupture plan that daylights downslope in the same daylight point D, is tightly dependent on the way to determine the downslope points below the rupture point. First, for efficiency reasons, we use the hydrologic graph, obtained by single flow algorithm based on the steepest slope criterion (O'Callaghan and Mark, 1984), to list the downslope points. On top of its computational efficiency, considering the geometry of hillslopes along hydrological paths was deemed relevant to assess the stability of hillslopes over large DEMs (Townsend et al., 2020; Medwedeff et al., 2020). We acknowledge that a more exhaustive but probably also less tractable search for the list of downslope points can be conceived, for instance allowing cross-divide landslides. Second, the approach is sensitive to the location of the fluvial or colluvial networks, here determined based on a critical drainage area, which delimits the base of the hillslope domain. Third, this approach also strongly depends on the resolution and accuracy of the DEM, with high resolutions probably leading to the identification of more numerous small landslides that may be simple artifacts due to topographic noise or local slope variability. Last, this approach does not explicitly check the resulting geometrical consistency of each individual landslide, and local particular topographic configuration could result in some local unrealistic landslide geometries.

4.2 A conundrum: realistic predictions of the number of landslides, landslide geometrical scaling laws and size distribution?

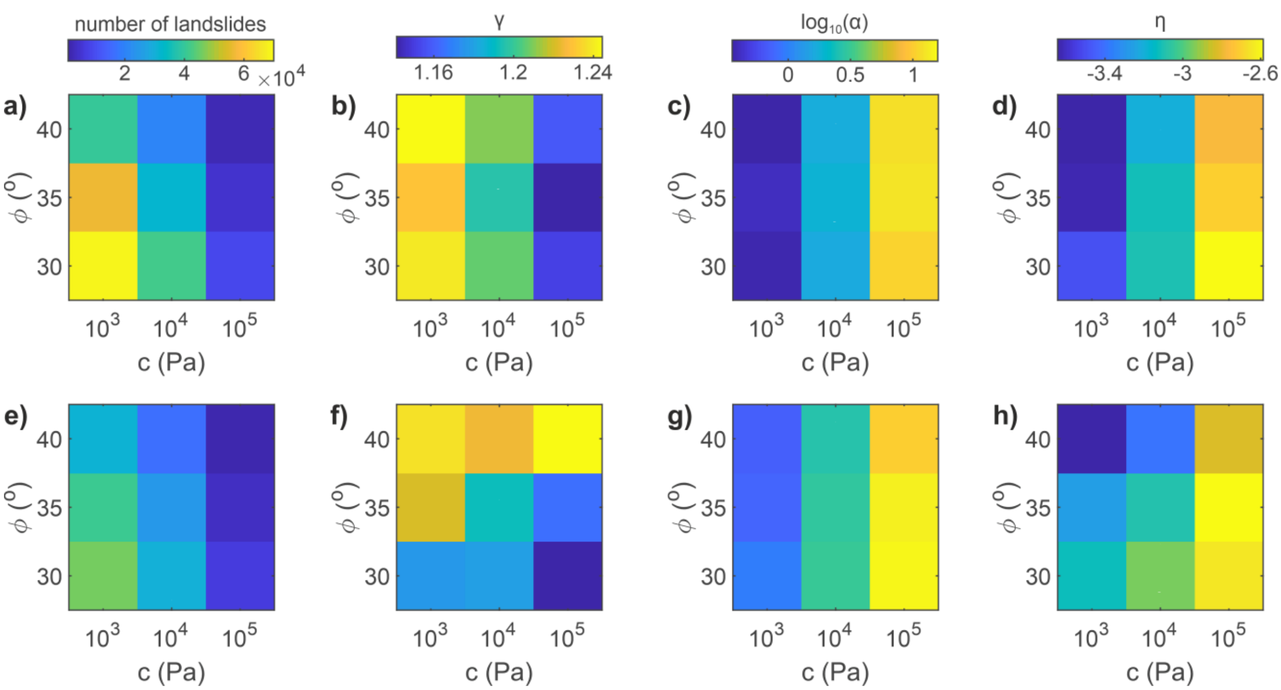

Figure 9: Sensitivity of the number of modelled landslides and their geometrical properties to the friction angle φ and cohesion c. a,e) Number of triggered landslides; b,f) Exponent γ of the V-A scaling relationship; c,g) Logarithm of the intercept $\log\alpha$ of the V-

https://doi.org/10.5194/egusphere-2026-4142
Preprint. Discussion started: 30 July 2026

A scaling relationship; d,h) Power-law exponent η of pdf(A) for large landslides. Upper panels (a-d) and lower panels (e-h) show the results for the initial and amalgamated landslides, respectively.

The reference model used for the Results section, predicted ~56,000 landslides (~41,000 for amalgamated landslides), a $V = \alpha A^{\gamma}$ scaling relationship with $\gamma = 1.23$ and $\log \alpha = -0.39$ (or $\gamma = 1.15$ and $\log \alpha = -0.12$), consistent with former studies (e.g., Larsen et al., 2010; Bernard et al, 2021), but a power-law exponent η=-3.6 (or η=-3.1) for the tail of the $pdf(A)$, which significantly differs from values obtained in Taiwan. This is achieved considering $c = 1$ kPa and $\varphi = 35°$. We here test the sensitivity of these results to varying c and φ, to investigate if a better representation of the distribution of landslide area can be achieved while keeping a good description of the V-A relationship. We vary c in the range 1-100 kPa and φ between 30 and 40° and focus only on the initial non-amalgamated landslides (as the results are rather similar for the amalgamated landslides). The number of landslides significantly decreases from ~68,000 to ~2,000 when increasing cohesion and friction or the overall strength of the hillslopes. The scaling exponent of the V-A relationship γ does not vary significantly, between 1.14 and 1.24, and roughly remains in the range of acceptable values 1.17 and 1.36 for mixed soil and bedrock landslides (Larsen et al., 2010; Bernard et al., 2021). We find that γ mostly vary with c, with lower values found for lower c values. The intercept α of the V-A relationship increases significantly with c, between $\log \alpha \approx -0.4$ and 1.0. Despite the significant variability observed in natural system, a realistic range for $\log \alpha$ is between -1.0 and 0.0 (Larsen et al., 2010), which excludes models with $c \geq 10$ kPa. This is problematic as we observe that the power-law exponent η of the tail of $pdf(A)$ also increases with c but reaches more realistic value for Taiwan, near $\eta \approx -2.5$, only when $c = 100$ kPa. This therefore means that the developed model does not successfully compare to all the natural constraints on landslide size and geometry for a single parametrization. Yet we also emphasize that 1) the obtained range for η, between -3.6 and -2.6, is roughly in the ranges of observed values based on various landslides catalogs worldwide between -1.4 and -3.5 (Van Den Eeckhaut et al., 2007) or -1.8 and -3.3 (Tanyas et al., 2019), and 2) the inherent amalgamation of natural landslides is a clear limitation when comparing modelled and natural landslides. This latter argument is illustrated by the difference in η between-3.6 and -3.1, when considering either the initial modelled landslides or the amalgamated ones, respectively. Moreover, the area distribution of amalgamated landslides provides a better fit to observation. This is even more reassuring as amalgamation is here performed based on a connected component approach, which is clearly not the most suitable approach to do this operation, despite its simplicity (Bernard et al., 2021).

4.3 No rollover for small landslides?

We also note that the modelled area distribution does not clearly display a rollover for small landslide areas, even if a break in slope occurs below a cutoff area (Fig. 8). Changing either cohesion or the friction angle, in the same ranges as in previous section, never leads to the emergence of a rollover. Obviously, the coarse resolution used in this study, 30 m (i.e., 900 m^2 for pixel size), does not help to resolve the occurrence or not of a rollover. However, we note that if we do systematically observe a break in slope for $pdf(A)$ below a cutoff area, no model shows a progressive decrease in slope towards low area which could suggest the presence of a rollover. Our modelling approach, which extends the work of Jeandet et al. (2019), shows different

https://doi.org/10.5194/egusphere-2026-4142
Preprint. Discussion started: 30 July 2026

results as rollover systematically emerged in this previous study. However, Jeandet et al. (2019) considered a probabilistic approach where each couple of rupture depth and angle was considered, while our approach is deterministic in the sense that only an optimal (i.e., most unstable) couple of depth and angle is considered for each point of the DEM. Jeandet et al. (2019) also do not explicitly modelled landslide lateral extent, which rather emerged in their approach due to the conversion of depth to area using a classical scaling law.

Whether landslide area distributions should theoretically display such a rollover is an active matter of debate (e.g., Stark & Hovius, 2001; Tanyas et al., 2019; Bernard et al., 2021). We refer the reader to Tebbens (2020) which offers a review of arguments for and against the occurrence of a rollover. A strong argument for the occurrence of a rollover is its presence in most landslide catalogs obtained from 2D imagery. However, a recent landslide catalog obtained from a direct 3D comparison of the topography, obtained by aerial Lidar, before and after the Kaikoura earthquake does not show a rollover, even for landslide area as low as 20 m^2 (Bernard et al., 2021). This is in contrast with two landslide catalogs obtained from 2D imagery in the same area which both exhibit a rollover located around 50-100 m^2 (Massey et al., 2020; Bernard et al., 2021). Our modelling results are therefore consistent (or at least not contradictory) with the results of Bernard et al. (2021), which probably represents the most compelling field evidence of the absence of a rollover.

4.4 Optimal rupture depth as a marker of landscape transience and crest disequilibrium?

We now qualitatively investigate the relationship between optimal rupture depth h_{min} and landscape transience (Fig. 10), applied to our study area (Fig. 3). In particular, we focus on the relative spatial distribution of h_{min} and of the normalized river steepness index (e.g., Kirby & Whipple, 2012), defined as $k_{sn} = S/A^{-\theta}$, with S the local river slope, A drainage area and $\theta = 0.5$ the concavity chosen here to match previous studies in this area (Chen & Willett, 2016; Chen et al., 2023). Local positive anomalies of k_{sn} (i.e., indicative of too strong slopes respectively to their local drainage area) can be indicative of upward migrating knickpoints or knickzones, driving higher rates of river incision. Rivers being the local baselevel of hillslopes, an increase in incision rates should lead to a steepening of hillslopes and to an increase in landslide activity (e.g., Berlin & Anderson, 2009; Gallen et al., 2011; Baynes et al., 2022; Soen et al., 2026). In turn, we expect to observe unstable slopes just uphill of these positive anomalies in k_{sn}, potentially also resulting in deeper rupture depths. This is indeed what can be qualitatively observed on Figure 10a. The broad pattern shows a global increase in k_{sn} from the west toward the main central divide of Taiwan, which correlates with more and deeper landslide instabilities. Then, local positive anomalies in k_{sn} are also associated with deeper rupture depths initiating at the hillslope toe and - potentially but not systematically - reaching the hillslope crest. These areas prone to deeper ruptures could be diagnosed as resulting from the propagation of river transience. Yet, compared to simply assessing hillslope steepening, h_{min} offers a physics-based metric which assesses the depth of gravitational instabilities driven by local slope but also by downhill topographic distribution.

https://doi.org/10.5194/egusphere-2026-4142
Preprint. Discussion started: 30 July 2026

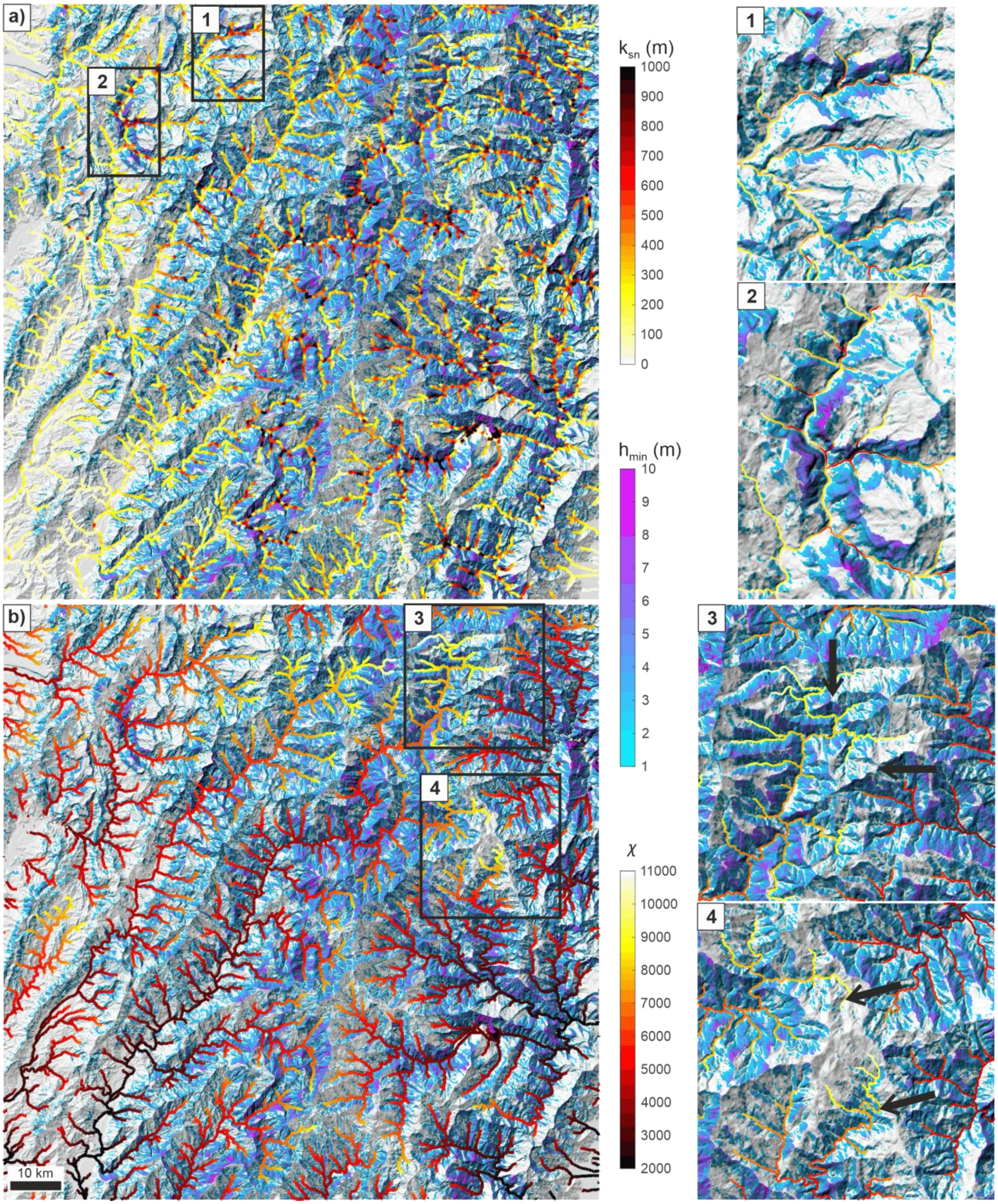

https://doi.org/10.5194/egusphere-2026-4142
Preprint. Discussion started: 30 July 2026

Figure 10: Maps of modelled landslide rupture depth compared to metrics of landscape transience. A) Map of the optimal rupture depth h_{min} (cool colormap) and of k_{sn} along the fluvial network (inverted hot colormap) in the studied area. Two locations associated with both high k_{sn} and high h_{min} are highlighted with black rectangles and a zoom is shown on the right of the figure. B) Map of the optimal rupture depth h_{min} (cool colormap) and of χ along the fluvial network (hot colormap) in the studied area. Two locations with divides marked by stark contrast in both χ and in the distribution of h_{min} are identified using black boxes and a zoom is shown on the right of the figure. The direction of the expected divide migration (from low to high values of χ) is shown by black arrows. Note that values of h_{min} are shown (above 1 m) only when they are associated with $F_{min} < 1$. χ was computed on the entire Taiwan island to ensure that all rivers share the same baselevel elevation (i.e., sea level).

We then test the ability of the developed algorithm to identify divide asymmetry and potential migration (Fig. 10b). In particular, the distribution of h_{min} and its potential asymmetric distribution along main divides offers means to assess potential migration of the divide resulting from hillslope failure. We assess the consistency of predicted divide asymmetry, from h_{min}, with the spatial distribution of χ (Perron & Royden, 2013) in the studied area. This index is computed as $\chi = \int_{x_b}^{x} \left(\frac{A_0}{A(x)}\right)^{\theta} dx$, with x the upstream distance along the fluvial network, x_b a reference location at the base of the fluvial network and $A_0 = 1$ km^2 a reference drainage area. Note that the χ analysis was made on the entire Taiwan island, using sea level as baselevel. χ predicts the horizontal coordinate that a river should take if at steady state.

As shown by previous studies, asymmetry in the distribution of χ between two sides of a divide can be cautiously interpreted as a marker of potential horizontal divide migration (e.g., Willet et al., 2014). The migration direction is supposed to go from the side with the low value of χ (i.e., the aggressor) to the side with the high value of χ (i.e., the victim). However, one relative weakness of using χ (i.e., fluvial metrics) to assess divide migration is that it assumes that hillslope processes respond linearly to river asymmetry. As shown by Chen et al. (2023), this hypothesis is reasonable as the distribution of landslides along the two sides of a divide tends to follow the asymmetric distribution of χ, with more landslides on the side with lower values of χ. We also observe that the distribution of h_{min} along divides marked by a strong asymmetry in χ, tends to be asymmetric, with higher values of h_{min} on the side of the divide associated with lower values of χ. We note that compared to high values of h_{min} observed at the hillslope toes and associated with high values of k_{sn}, asymmetric divides are mostly characterized with high values of h_{min} reaching the divide on the aggressor side, which could indicate a future migration of divide line associated to greater landslide depth on the aggressor side. Yet, this consistency between these two indices is not systematic, and a more thorough investigation is needed. This still offers an interesting perspective for future study on divide migration, as h_{min} offers a complementary index to χ, that is potentially more informative on mass wasting processes and their potential depth amplitude along hillslopes. With this regard, the optimal rupture depth h_{min} could be considered in line with some Gilbert metrics (Gilbert, 1877), such as the cross-divide difference in mean headwater hillslope gradient, except that it is derived from the physics of hillslope stability and brings a quantification of the expected topographic change. These metrics inform on current divide migration, likely driven by landsliding and mass wasting processes in steep landscapes, while χ could inform on future migration (Forte & Whipple, 2018).

https://doi.org/10.5194/egusphere-2026-4142
Preprint. Discussion started: 30 July 2026

5 Conclusion

In this study, we have developed a new landslide model that extends previous works, in particular Jeandet et al. (2019), trying to understand how mechanical stability and topographic constraints impact the size distributions and geometrical scaling laws of landslides. Our approach is based on the analytical solution for the optimal rupture depth at which a point should fail, which is imposed by the surface geometry of the rupture plane and the location of where this plane daylights downslope. Interestingly, we find that unstable points tend to share locally similar daylight points, and that these clusters of points form 3D geometrical shapes with a size distribution and geometrical scaling laws which are consistent with natural landslides (e.g., Larsen et al., 2010 Bernard et al., 2021; Van Den Eeckhaut et al., 2007; Tanyas et al., 2019). Following previous studies (e.g., Alvioli et al., 2014), our results suggest that landslides might therefore emerge as spatially continuous patches of unstable neighborhood points. We apply our model to the Central Range of Taiwan, a landslide-prone area. We find a good consistency between statistical properties of modelled landslides and natural ones when considering their area-volume relationships, area-depth relationships and possibly the distributions of landslides length-to-width ratios (which is less well constrained). However, if we obtain a satisfactory overall distribution of landslide area, modelled landslide areas tend to follow a steeper power-law decay than natural ones. Better landslide area distributions can be obtained when changing the mechanical parameters of the model, but this also decreases the consistency of the area-volume relationship. We illustrate that the lack of landslide amalgamation in the modelled landslide catalog might at least partly explain this mismatch. The modeled distributions of landslide area do not show any rollover for small landslide area, which is consistent with recent observations (Bernard et al., 2021) but differ from several previous papers. Lastly, we show that the optimal rupture depth can be considered as a physics-based morphometric index to detect, along hillslopes, landscape transience resulting from divide migration or knickpoint propagation. This opens new perspectives to integrate hillslope mass wasting processes in morphometric studies.

Appendix A: Extending the approach to account for hydrostatic pore pressure

As shown in the Methods section, finding the depth h_{min} that minimises the safety factor can be solved analytically when above the water table or when no water table is considered (Eq. 5,6). However, when accounting for hydrostatic pore pressure associated with the water table, the solution becomes significantly more complex. In the following, we define d as the depth of the water table below the topography. Pore pressure ψ is expressed under hydrostatic conditions at any depth h, below the water table, as $\psi = \rho_w g(h-d)$, with ρ_w the water density. The hydrostatic load of the height of water is added as pore pressure into the safety factor:

$$F = \frac{c + \mu(\sigma_n - \psi)}{\tau} \qquad (A1)$$

Developing the expression of the safety factor leads to:

$$F = \frac{c}{\rho g h}\frac{\Delta x^2 + (\Delta z - h)^2}{\Delta x(\Delta z - h)} + \mu\frac{\Delta x}{\Delta z - h} - \frac{\rho_w}{\rho}\mu(h-d)\frac{\Delta x^2 + (\Delta z - h)^2}{\Delta x(\Delta z - h)} \qquad (A2)$$

The derivative of F relative to h can be obtained:

https://doi.org/10.5194/egusphere-2026-4142
Preprint. Discussion started: 30 July 2026

$$\frac{dF}{dh} = \frac{c}{\rho g h}\left(\frac{\Delta x^2 + (\Delta z - h)^2}{\Delta x(\Delta z - h)^2} - \frac{2(\Delta z - h)}{\Delta x(\Delta z - h)} - \frac{\Delta x^2 + (\Delta z - h)^2}{\Delta x(\Delta z - h)h}\right) + \mu\frac{\Delta x}{(\Delta z - h)^2}$$
$$-\mu\frac{\rho_w}{\rho}\frac{(-\Delta x)h^4 + (2\Delta x\Delta z)h^3 + (\Delta x^3 - \Delta x\Delta z^2 + \Delta x\Delta z d)h^2 + (2\Delta x\Delta z d - 2\Delta x^3 d - 4\Delta x\Delta z^2)h + (\Delta x^3\Delta z d + \Delta x\Delta z^3 d)}{\Delta x^2 h^4 - 2\Delta x^2\Delta z h^3 + \Delta x^2\Delta z^2 h^3} \quad (A3)$$

One can note that the first two terms of Eq. (A3) are identical to Eq. (4), expressed without the contribution of hydrostatic pore pressure. However, the last term, a polynomial of degree 4, appears due to the contribution of hydrostatic pore pressure. Solving for the roots of $\frac{dF}{dh}$ should provide with analytical expressions of h_{min}. However, the solution to this equation is not trivial, and solving it by hand, while theoretically possible, is realistically not feasible. The software Maple solves the equation and provides its 4 roots. The solution will however not be presented here, because, to quote Pierre de Fermat, "*I have discovered a truly marvellous proof of this, which this margin is too narrow to contain.*" would be an understatement. Indeed, the full solution represent a little less than 200,000 characters and is quite unpractical to use. Therefore, instead of using analytical solutions to determine h_{min}, a numerical algorithm can be developed to approximate the solution. For instance, for each potential rupture point R, and for every possible daylight point D, the safety factor is evaluated along the depth at regular intervals, and the depth leading to the minimum value of F is considered as the optimal rupture depth. More sophisticated numerical scheme can be introduced, but the computation time and the memory requirements can easily become a main limitation when applied to large DEMs. The depth of the water table can then be either extrapolated from field data, approximated using simple formalisms (e.g., Townley, 1995) or computed using 2 or 3D numerical models (e.g., Abhervé et al., 2022).

Code availability. The scaLr Matlab model can be found here: https://github.com/philippe-steer/scaLr

Author contribution. PS conceived the study and developed the methodology. LP developed the solution when accounting for pore pressure. PS prepared the manuscript with contributions from LP and LL.

Competing interests. The authors declare that they have no conflict of interest.

Acknowledgments. We are grateful to Louise Jeandet, Dimitri Lague, Philippe Davy, Clément Desormeaux, Marin Clark and the FRES team for discussions and insights on landslide modelling.

Funding support. This research has been supported by the H2020 European Research Council (grant no. 803721) and the Institut Universitaire de France (IUF).

https://doi.org/10.5194/egusphere-2026-4142
Preprint. Discussion started: 30 July 2026

References

Abhervé, R., Gauvain, A., Roques, C., Longuevergne, L., Louaisil, S., Aquilina, L., & de Dreuzy, J. R.: Calibration of groundwater seepage on the spatial distribution of the stream network to assess catchment-scale hydraulic conductivity, Hydrology and Earth System Sciences Discussions, 1-26, 2022.

Alberti, S., Leshchinsky, B., Roering, J., Perkins, J., & Olsen, M. J.: Inversions of landslide strength as a proxy for subsurface weathering, Nature Communications, 13(1), 6049, 2022.

Alvioli, M., Guzzetti, F., & Rossi, M.: Scaling properties of rainfall induced landslides predicted by a physically based model, Geomorphology, 213, 38-47, 2014.

Argentin, A. L., Hauthaler, T., Liebl, M., Robl, J., Hergarten, S., Prasicek, G., ... & Dabiri, Z.: Influence of rheology on landslide-dammed lake impoundment and sediment trapping: Back-analysis of the Hintersee landslide dam, Geomorphology, 414, 108363, 2022.

Bak, P.: How Nature Works: The Science of Self-Organized Criticality, Springer, Berlin. http://dx.doi.org/10.1007/978-1-4757-5426-1, 1996

Baynes, E. R., Lague, D., Steer, P., & Davy, P.: Dynamic bedrock channel width during knickpoint retreat enhances undercutting of coupled hillslopes, Earth Surface Processes and Landforms, 47(15), 3629-3640, 2022.

Bellugi, D., Milledge, D. G., Dietrich, W. E., Perron, J. T., & McKean, J.: Predicting shallow landslide size and location across a natural landscape: Application of a spectral clustering search algorithm, Journal of Geophysical Research: Earth Surface, 120(12), 2552-2585, 2015.

Bellugi, D. G., Milledge, D. G., Cuffey, K. M., Dietrich, W. E., & Larsen, L. G.: Controls on the size distributions of shallow landslides, Proceedings of the National Academy of Sciences, 118(9), e2021855118, 2021.

Berlin, M. M., & Anderson, R. S.: Steepened channels upstream of knickpoints: Controls on relict landscape response, Journal of Geophysical Research: Earth Surface, 114(F3), 2009.

Bernard, T. G., Lague, D., & Steer, P.: Beyond 2D landslide inventories and their rollover: synoptic 3D inventories and volume from repeat lidar data, Earth Surface Dynamics, 9(4), 1013-1044, 2021.

Campforts, B., Shobe, C. M., Steer, P., Vanmaercke, M., Lague, D., & Braun, J.: HyLands 1.0: a hybrid landscape evolution model to simulate the impact of landslides and landslide-derived sediment on landscape evolution, Geoscientific Model Development, 13(9), 3863-3886, 2020.

Casadei, M., Dietrich, W. E., & Miller, N. L.: Testing a model for predicting the timing and location of shallow landslide initiation in soil-mantled landscapes, Earth Surface Processes and Landforms: The Journal of the British Geomorphological Research Group, 28(9), 925-950, 2003.

Chen, C. Y., & Willett, S. D.: Graphical methods of river profile analysis to unravel drainage area change, uplift and erodibility contrasts in the Central Range of Taiwan, Earth Surface Processes and Landforms, 41(15), 2223-2238, 2016.

https://doi.org/10.5194/egusphere-2026-4142
Preprint. Discussion started: 30 July 2026

Chen, C. H., Shyu, J. B. H., Willett, S. D., & Chen, C. Y.: Structural control on drainage pattern development of the western Taiwan orogenic wedge, Earth Surface Processes and Landforms, 2023.

Clark, M. K., Zekkos, D., & Manousakis, J.: Enabling 3D landslide event statistics using satellite and UAV-enabled topographic differencing, Landslides, 22(4), 1041-1058, 2025.

Croissant, T., Steer, P., Lague, D., Davy, P., Jeandet, L., & Hilton, R. G.: Seismic cycles, earthquakes, landslides and sediment fluxes: Linking tectonics to surface processes using a reduced-complexity model, Geomorphology, 339, 87-103, 2019.

Croissant, T., Hilton, R. G., Li, G. K., Howarth, J., Wang, J., Harvey, E. L., ... & Densmore, A. L.: Pulsed carbon export from mountains by earthquake-triggered landslides explored in a reduced-complexity model, Earth Surface Dynamics, 9(4), 823-844, 2021.

Densmore, A. L., Ellis, M. A., & Anderson, R. S.: Landsliding and the evolution of normal-fault-bounded mountains, Journal of geophysical research: solid earth, 103(B7), 15203-15219, 1998.

Dietrich, W. E., McKean, J., Bellugi, D., & Perron, T.: The prediction of shallow landslide location and size using a multidimensional landslide analysis in a digital terrain model, In Proceedings of the Fourth International Conference on Debris-Flow Hazards Mitigation: Mechanics, Prediction, and Assessment (DFHM-4) (pp. 10-13), Amsterdam, The Netherlands: IOS Press, 2007.

Forte, A. M., & Whipple, K. X.: Criteria and tools for determining drainage divide stability, Earth and Planetary Science Letters, 493, 102-117, 2018.

Frattini, P., & Crosta, G. B.: The role of material properties and landscape morphology on landslide size distributions, Earth and Planetary Science Letters, 361, 310-319, 2013.

Gallen, S. F., Clark, M. K., & Godt, J. W.: Coseismic landslides reveal near-surface rock strength in a high-relief, tectonically active setting, Geology, 43(1), 11-14, 2015.

Gilbert, G. K.: Geology of the Henry Mountains, USGS Report, Government Printing Office, Washington, D.C., 1877.

Gong, W., Zekkos, D., & Clark, M.: The influence of seismic displacement models on spatial prediction of regional earthquake-induced landslides, Engineering Geology, 325, 107288, 2023.

Guzzetti, F., Reichenbach, P., Cardinali, M., Galli, M., & Ardizzone, F.: Probabilistic landslide hazard assessment at the basin scale, Geomorphology, 72(1-4), 272-299, 2005.

Guzzetti, F., Ardizzone, F., Cardinali, M., Rossi, M., & Valigi, D.: Landslide volumes and landslide mobilization rates in Umbria, central Italy, Earth and Planetary Science Letters, 279(3-4), 222-229, 2009.

Hergarten, S.: Self organized criticality in earth systems (Vol. 2, No. 2). Berlin: Springer, 2002.

Hilton, R. G., Galy, A., & Hovius, N.: Riverine particulate organic carbon from an active mountain belt: Importance of landslides. Global Biogeochemical Cycles, 22(1), 2008.

Hovius, N., Stark, C. P., & Allen, P. A.: Sediment flux from a mountain belt derived by landslide mapping, Geology, 25(3), 231-234, 1997.

https://doi.org/10.5194/egusphere-2026-4142
Preprint. Discussion started: 30 July 2026

Huber, M., Scholtes, L., & Lavé, J.: Stability and failure modes of slopes with anisotropic strength: Insights from discrete element models, Geomorphology, 444, 108946, 2024.

Hurst, M. D., Grieve, S. W., Clubb, F. J., & Mudd, S. M.: Detection of channel-hillslope coupling along a tectonic gradient, Earth and Planetary Science Letters, 522, 30-39, 2019.

Jaboyedoff, M., Carrea, D., Derron, M. H., Oppikofer, T., Penna, I. M., & Rudaz, B.: A review of methods used to estimate initial landslide failure surface depths and volumes, Engineering Geology, 267, 105478, 2020.

Jeandet, L., Steer, P., Lague, D., & Davy, P.: Coulomb mechanics and relief constraints explain landslide size distribution, Geophysical Research Letters, 46(8), 4258-4266, 2019.

Jones, K. E., Howarth, J. D., Massey, C. I., Luković, B., Sirguey, P., Singeisen, C., Gasston, C., Morgenstern, R., & Ries, W.: An alternative to landslide volume-area scaling relationships: an ensemble approach adopting a difference model to estimate the total volume of landsliding triggered by the 2016 Kaikōura earthquake, New Zealand, Landslides, 22(7), 2219-2236, 2025.

Ju et al., 2023; Ju, L. Y., Zhang, L. M., & Xiao, T.: Power laws for accurate determination of landslide volume based on high-resolution LiDAR data, Engineering Geology, 312, 106935, 2023.

Kearney, W., Arnau, G., Bringezu, T., Dietze, M., Gailleton, B., Lamprecht, A.-L., Lenz, K., Ott, R., Scherler, D., Steer, P., & Schwanghart, W.: TopoToolbox 3, a laboratory for quantitative geomorphology, EGUsphere, 2026.

Keefer, D. K.: The importance of earthquake-induced landslides to long-term slope erosion and slope-failure hazards in seismically active regions. In Geomorphology and natural hazards (pp. 265-284). Elsevier, 1994.

Kirby, E., & Whipple, K. X.: Expression of active tectonics in erosional landscapes, Journal of structural geology, 44, 54-75, 2012.

Klar, A., Aharonov, E., Kalderon-Asael, B., & Katz, O.: Analytical and observational relations between landslide volume and surface area, Journal of Geophysical Research: Earth Surface, 116(F2), 2011.

Kuo, C. Y., Tai, Y. C., Bouchut, F., Mangeney, A., Pelanti, M., Chen, R. F., & Chang, K. J.: Simulation of Tsaoling landslide, Taiwan, based on Saint Venant equations over general topography, Engineering Geology, 104(3-4), 181-189, 2009.

Lague, D., & Davy, P.: Constraints on the long-term colluvial erosion law by analyzing slope-area relationships at various tectonic uplift rates in the Siwaliks Hills (Nepal), Journal of Geophysical Research: Solid Earth, 108(B2), 2003.

Larsen, I. J., Montgomery, D. R., & Korup, O.: Landslide erosion controlled by hillslope material, Nature Geoscience, 3(4), 247-251, 2010.

Lavé, J., Guérin, C., Valla, P. G., Guillou, V., Rigaudier, T., Benedetti, L., ... & Galy, V.: Medieval demise of a Himalayan giant summit induced by mega-landslide, Nature, 619(7968), 94-101, 2023.

Lehmann, P., & Or, D.: Hydromechanical triggering of landslides: From progressive local failures to mass release, Water Resources Research, 48(3), 2012.

Lucas, A., Mangeney, A., Mège, D., & Bouchut, F.: Influence of the scar geometry on landslide dynamics and deposits: Application to Martian landslides, Journal of Geophysical Research: Planets, 116(E10), 2011.

Malamud, B. D., & Turcotte, D. L. : Self-organized criticality applied to natural hazards, Natural Hazards, 20, 93-116, 1999.

Malamud, B. D., Turcotte, D. L., Guzzetti, F., & Reichenbach, P.: Landslide inventories and their statistical properties, Earth Surface Processes and Landforms, 29(6), 687-711, 2004.

Marc, O., Behling, R., Andermann, C., Turowski, J. M., Illien, L., Roessner, S., & Hovius, N.: Long-term erosion of the Nepal Himalayas by bedrock landsliding: the role of monsoons, earthquakes and giant landslides, Earth Surface Dynamics, 7(1), 107-128, 2019.

Medwedeff, W. G., Clark, M. K., & Zekkos, D.: Regional back-analysis of earthquake triggered landslide inventories: A 2D method for estimating rock strength from remote sensing data, Journal of Geophysical Research: Earth Surface, 130(1), e2023JF007471, 2025.

Medwedeff, W. G., Clark, M. K., Zekkos, D., & West, A. J.: Characteristic landslide distributions: An investigation of landscape controls on landslide size, Earth and Planetary Science Letters, 539, 116203, 2020.

Milledge, D. G., Bellugi, D., McKean, J. A., Densmore, A. L., & Dietrich, W. E.: A multidimensional stability model for predicting shallow landslide size and shape across landscapes, Journal of Geophysical Research: Earth Surface, 119(11), 2481-2504, 2014.

Montgomery, D. R., & Foufoula-Georgiou, E.: Channel network source representation using digital elevation models, Water Resources Research, 29(12), 3925-3934, 1993.

Moretti, L., Allstadt, K., Mangeney, A., Capdeville, Y., Stutzmann, E., & Bouchut, F.: Numerical modeling of the Mount Meager landslide constrained by its force history derived from seismic data, Journal of Geophysical Research: Solid Earth, 120(4), 2579-2599, 2015.

O'Callaghan, J. F., & Mark, D. M.: The extraction of drainage networks from digital elevation data, Computer vision, graphics, and image processing, 28(3), 323-344, 1984.

Pelletier, J. D., Malamud, B. D., Blodgett, T., & Turcotte, D. L.: Scale-invariance of soil moisture variability and its implications for the frequency-size distribution of landslides, Engineering Geology, 48(3-4), 255-268, 1997.

Perron, J. T., & Royden, L.: An integral approach to bedrock river profile analysis, Earth surface processes and landforms, 38(6), 570-576, 2013.

Phillips, C., Hales, T., Smith, H., & Basher, L.: Shallow landslides and vegetation at the catchment scale: A perspective, Ecological Engineering, 173, 106436, 2021.

Samyn, K., Travelletti, J., Bitri, A., Grandjean, G., & Malet, J. P.: Characterization of a landslide geometry using 3D seismic refraction traveltime tomography: The La Valette landslide case history, Journal of Applied Geophysics, 86, 120-132, 2012.

Schwanghart, W., & Scherler, D.: TopoToolbox 2–MATLAB-based software for topographic analysis and modeling in Earth surface sciences, Earth Surface Dynamics, 2(1), 1-7, 2014.

Stark, C. P., & Guzzetti, F.: Landslide rupture and the probability distribution of mobilized debris volumes, Journal of Geophysical Research: Earth Surface, 114(F2), 2009

Stark, C. P., & Hovius, N.: The characterization of landslide size distributions, Geophysical research letters, 28(6), 1091-1094, 2001.

https://doi.org/10.5194/egusphere-2026-4142
Preprint. Discussion started: 30 July 2026

Steer, P., Jeandet, L., Cubas, N., Marc, O., Meunier, P., Simoes, M., ... & Hovius, N.: Earthquake statistics changed by typhoon-driven erosion, Scientific reports, 10(1), 10899, 2020.

Steer, P.: Analytical models for 2D landscape evolution, Earth Surface Dynamics, 9(5), 1239-1250, 2021.

Suen, M. H., Naylor, M., Mudd, S. M., & Lindgren, F.: Influence of river incision on landslides triggered in Nepal by the 2015 Gorkha earthquake: Results from a pixel-based susceptibility model using inlabru, Frontiers in Earth Science, 14, 1876760, 2026

Tanyaş, H., van Westen, C. J., Allstadt, K. E., Anna Nowicki Jessee, M., Görüm, T., Jibson, R. W., ... & Hovius, N.: Presentation and analysis of a worldwide database of earthquake-induced landslide inventories, Journal of Geophysical Research: Earth Surface, 122(10), 1991-2015, 2017.

Tanyaş, H., van Westen, C. J., Allstadt, K. E., & Jibson, R. W.: Factors controlling landslide frequency–area distributions, Earth surface processes and landforms, 44(4), 900-917, 2019.

Taylor, F. E., Malamud, B. D., Witt, A., & Guzzetti, F.: Landslide shape, ellipticity and length-to-width ratios, Earth Surface Processes and Landforms, 43(15), 3164-3189, 2018.

Tebbens, S. F.: Landslide scaling: a review, Earth and Space Science, 7(1), e2019EA000662, 2020.

Townley, L. R.: The response of aquifers to periodic forcing, Advances in water Resources, 18(3), 125-146, 1995.

Townsend, K. F., Gallen, S. F., & Clark, M. K.: Quantifying near-surface rock strength on a regional scale from hillslope stability models, Journal of Geophysical Research: Earth Surface, 125(7), e2020JF005665, 2020.

Van Den Eeckhaut, M., Poesen, J., Govers, G., Verstraeten, G., & Demoulin, A.: Characteristics of the size distribution of recent and historical landslides in a populated hilly region, Earth and Planetary Science Letters, 256(3-4), 588-603, 2007.

Willett, S. D., McCoy, S. W., Perron, J. T., Goren, L., & Chen, C. Y.: Dynamic reorganization of river basins, Science, 343(6175), 1248765, 2014.